Journal of Advanced Environmental Research and Technology

jaert.modares.ac.ir

Hydrophobic Membranes in Oily Wastewater Treatment: 3D COMSOL Simulation Approach

Fariba Khalili [1,*]

[1] *Department of Chemical Engineering, Shiraz Branch, Islamic Azad University, Shiraz, Iran.*

Article info

Received 2024-06-27
Revised 2024-02-21
Accepted 2024-02-21

Abstract

This study explores the filtration performance of hollow fiber hydrophobic ceramic membranes for treating oily wastewater in petroleum, chemical, and food industries using 3D simulations in COMSOL Multiphysics. The model simulates water as the continuous phase and oil as a dispersed phase with a concentration of less than 4%. The governing equations are based on Eulerian multi-phase flow theory, Darcy's Law, and the porous media model, solved using the finite element method. Key parameters affecting membrane separation performance, including velocities, cake thickness, and permeate concentration, are analyzed across different injection flow rates, transmembrane pressures, oil concentrations, and size distributions. Results indicate that increasing the permeation pressure increases the oil concentration in the permeate, resulting in a thinner, denser oil layer. A higher injection flow rate and oil concentration also lead to increased permeate oil concentration. The simulation results align well with laboratory data, demonstrating the effectiveness of the chosen.

Keywords

Membranes
Oil-water separation
Numerical simulation
Eulerian multi-phase flow
hydrophobic ceramic membranes
COMSOL
simulation.

---

* Corresponding author: fariba.khalili@iau.ac.ir

DOI: ……..

1. Introduction

Oil-contaminated water is one of the most common pollutants released into the environment by various industries, such as petroleum refining, petrochemicals, and manufacturing [1, 2]. Therefore, understanding the oil-water separation process is crucial for both industrial applications and environmental protection [3, 4]. According to the North-East Atlantic Convention for the Protection of the Marine Environment, the annual limit for oil discharge into the sea is 40 mg/L [5]. At this low concentration, where the oil droplets are very small, the process of separating oil from water becomes more complex, particularly for droplets smaller than 20 µm [6, 7].

Several conventional methods, including biological, chemical, physical, and physicochemical techniques [8], as well as nanofibril [9-11] and membrane filtration methods [12], are commonly employed to treat oily water [13].

Membrane materials are increasingly important in both industrial and everyday applications, particularly in water purification, desalination, and energy conversion [14]. The first efforts to purify oily water using membranes date back to the early 1970s [15]. Due to several advantages of membrane treatment, such as operational simplicity, low energy costs, long lifespan, high-quality permeate, no need for chemicals, biological stability, and resistance to high temperatures, membrane filtration has garnered significant interest from researchers over the last two decades [16]. However, challenges such as reduced permeate flow and the formation of polarization layers, caused by pore sedimentation, remain significant issues in membrane usage [7].

To better understand the performance of membrane contactor systems and the factors affecting their efficiency, numerous experimental [6, 17], mathematical [16], and numerical [18-20] studies have been conducted under both hydrophilic and hydrophobic conditions [3, 8, 9, 11, 12, 21-24]. These studies aim to provide insights into two-phase filtration systems, specifically oil-water filtration with membranes.

Due to limited laboratory equipment, the high costs of laboratory research, and the increased accuracy of advanced simulation tools, researchers are increasingly turning to simulation methods for studying membrane contactors. Computational fluid dynamics (CFD) has become a crucial tool for simulating flow in various systems [15]. Using CFD techniques, conservation equations, such as continuity, energy, and momentum balance equations, are solved numerically.

For simulating membrane contactors, the finite element method is commonly used to solve governing equations for species in all phases. Various membrane shapes, such as flat plates [7], circular or tubular membranes [13, 20], and annular membranes [16, 25], have been modeled in both two-dimensional [13, 25-28] and three-dimensional [5, 15] geometries.

In the literature, different simulation methods have been used for two-phase filtration through membranes, including the projection level set method, the volume of fluid method, and the population balanced model [29]. The resistance-in-series method is frequently employed to determine mass transfer in membrane contactors and to predict phase-specific mass transfer coefficients under steady-state conditions [30].

For CFD and numerical simulations of membrane contactors, ANSYS [13, 20, 29, 31] and COMSOL Multiphysics [29, 32-35] are two widely used tools. Several studies [19, 36] suggest that a combination of the Navier-Stokes and continuity equations, along with "Film Theory" based on rejection and permeation flux, results in more accurate flow patterns and pressure fields.

For simulating membrane contactors, axial diffusion is typically neglected for simplicity. For the gas-liquid and liquid-liquid interfaces, researchers have applied non-wetting conditions [13, 32, 37, 40] or partial and complete wetting conditions [41] as boundary conditions for membrane walls.

Most experimental and numerical investigations of membrane contactors focus on polymer [42] and ceramic membranes [13] in laminar flow regimes [16, 29, 43] as well as turbulent conditions [15].

This article presents a numerical study on the performance of an annular membrane filtration system for oil-water separation under steady-state, laminar flow conditions in a 3D simulation. The study uses the "Euler-based multiphase" model combined with Darcy's law, the "Free and Porous Media" boundary model, and the "Transport of Dilute Species" model, solved using COMSOL Multiphysics. This is the first application of this approach to simulate an annular hydrophobic ceramic membrane, investigating the effects of inlet flow rate and membrane diameter on performance. The resistance-in-series theory is applied to determine the local permeation rate for two-phase flows.

2. Theory

2.1. Module geometry

This study focuses on the modeling and performance simulation of oily water separation using an annular membrane tube, modeled with COMSOL Multiphysics. The inner diameter of the membrane was 0.03 m, with a thickness of 0.001 m and a length of 0.3 m. Surrounding the membrane, a shell with an inner diameter of 0.05 m was used to collect the separated oil. The system exhibits axial symmetry. The feed consisted of a mixture of water, acting as the continuous phase, and oil, the dispersed phase. The oil's density was assumed to be 850 kg/m³, and its viscosity was set at 0.00332 kg/m·s.

2.2. Governing equations

The mathematical model used to describe the water/oil flow inside the annular membrane system consists of the governing equations: the mass conservation equation [Eq. 1], the momentum conservation equation (Navier-Stokes) [Eq. 2], and the mass transport equation (Darcy's Law) [Eq. 3] [39]. All equations are formulated in Cartesian coordinates. In this study, water is considered the continuous phase, while oil is treated as the dispersed phase.

$$\frac{D\rho}{Dt} + \rho\nabla.\bar{U} = 0 \tag{1}$$

$$\rho\frac{D\bar{U}}{Dt} = -\nabla p - \nabla.\tau + \rho\bar{g} \tag{2}$$

$$\bar{U}.\nabla C = D_{AB}\nabla^2\mathrm{C} \tag{3}$$

Where ρ is the density, μ is the viscosity, and U is the velocity vector, defined as follows:

$$\bar{U} = (u(x,y,z), v(x,y,z), w(x,y,z)) \tag{4}$$

Where u, v, and w are the velocity components in the x, y, and z directions, respectively; C is the solute (oil) concentration; and D_{AB} is its mass diffusivity, assumed constant for a fixed Schmidt number (Sc), as follows:

$$D_{AB} = \frac{\mu}{S_{c\rho}} \tag{5}$$

For water, as the continuous phase, the numerical solutions of the mass [Eq. 1] and momentum [Eq. 2] conservation equations (Navier-Stokes), as well as the mass transport equation [Eq. 3], were used to describe the dominant inflow hydrodynamics [44]. The mixture formulation of the governing equations, based on Eulerian multiphase flow theory and relative velocity, was applied to the emulsified oil micelles in the dispersed phase, as follows:

$$\frac{\partial}{\partial t}(\rho_m\vec{v}_m) + \nabla.(\rho_m\vec{v}_m\vec{v}_m) = -\nabla p + \nabla.[\mu_m(\nabla v_m + \nabla\vec{v}_m^t)] + \rho_m g + \vec{F} + \nabla.(\textstyle\sum_{k=1}^{n}\alpha_k\rho_k\vec{v}_{drk}\vec{v}_{drk}) \tag{6}$$

$$\mu_m = \textstyle\sum_{k=1}^{n}\alpha_k\mu_k \tag{7}$$

$$\frac{\partial}{\partial t}(\rho_m) + \nabla.(\rho_m\vec{v}_m) = 0 \tag{8}$$

$$\vec{v}_m = \frac{\sum_{k=1}^{n}\alpha_k\rho_k\vec{v}_k}{\rho_m} \tag{9}$$

$$\rho_m = \sum_{k=1}^{n}\alpha_k\rho_k \tag{10}$$

$$\frac{\partial}{\partial t}(\alpha_o\rho_o) + \nabla.(\alpha_o\rho_o\vec{v}_m) = -\nabla.\left(\alpha_o\rho_o\vec{v}_{drp}\right) \tag{11}$$

$$\vec{v}_{drp} = \vec{v}_{wo} - \sum\alpha_o\vec{v}_{wk} \tag{12}$$

$$C_k = \frac{\alpha_k\rho_k}{\rho_m} \tag{13}$$

$$\vec{v}_{wo} = \vec{v}_o - \vec{v}_w = \frac{\tau_o}{f_{dr\,ag}}\frac{(\rho_o - \rho_m)}{\rho_o}\vec{a} \tag{14}$$

$$\tau_o = \frac{\rho_o d_o^2}{18\,\mu_o} \tag{15}$$

$$f_{drag} = \begin{cases} 1 + 0.15\,Re^{0.687} & Re \leq 1000 \\ 0.0183\,Re & Re > 1000 \end{cases} \tag{16}$$

$$\vec{a} = \vec{g} - (\vec{v}_m.\nabla)\vec{v}_m - \frac{\partial\vec{v}_m}{\partial t} \tag{17}$$

Where n is the number of phases (in this case, two phases), v_m, ρ_m, and μ_m represent the mass-averaged velocity, density, and viscosity of the mixture, respectively. α_k is the volume fraction of phase k, with the subscript w referring to water as the continuous phase and o representing oil as the dispersed phase. v_{drp} is the drift velocity, C_k is the mass fraction for phase k, and v_{ow} is the relative velocity. τo is the particle relaxation time, do is the mean particle diameter, f_{drag} is the drag coefficient, F is the body force, and a is the acceleration. The time-dependent terms were neglected in this study due to the steady-state condition of the problem. Through the porous wall, the radial velocity v is equal to the permeation velocity w, as follows:

$$v = w = \frac{\Delta P}{\mu(R)} \tag{18}$$

$$R = R_m + R_P \tag{19}$$

The transmembrane pressure ΔP or TMP in Equation 18 is defined as the difference between the mean permeate pressure, $\bar{P}_p$, and external pressure Pex.

$$TMP = \Delta P = \bar{P}_p - P_{ex} \tag{20}$$

In Equation 18, R is considered as the total resistance of the system and is equal to the summation of the membrane resistance *(Rm) and* concentration polarization resistance *(Rp)* defined as the following equations:

$$R_m = \frac{e}{K} \tag{21}$$

$$R_p = r_p \delta_p \tag{22}$$

K is the permeability, e is the thickness of the membrane, δ_p is the thickness of the concentration layer, and r_p is the resistance of the system, assuming the concentration layer is homogeneous. This parameter is defined by the Carman-Kozeny equation, as follows:

$$r_p = 180\frac{\left(1 - \varepsilon_p\right)^2}{d_n^2 \varepsilon_n^3} \tag{23}$$

Where ε_p is the porosity of the polarization layer by concentration (equal to 0.35), and *dp* is the mean diameter of the solute particles (Oil). The local variation of the polarization boundary layer thickness can be determined by Equation 24 as follows:

$$\frac{\delta_p}{d_i} = 2\left(\frac{z}{d_i}\right)^{0.33} (ReSc)^{-0.33} Re_w^{-0.3} [1 - 0.4377(Sc^{-0.0018} Re_w^{-0.1551})] \tag{24}$$

Where d_i is the internal diameter, z is the axial coordinate along the membrane, Re is the axial Reynolds number, Re_w is the Reynolds number at the wall permeate, and Sc is the Schmidt number.

2.3. Boundary conditions

In this problem, the system was divided into three zones: A, B, and C, as shown in Figure 1. The feed was considered to be premixed and homogeneous, with the same velocity assumed for both the continuous and dispersed phases. For simulation, the boundary condition at the inlet was defined by the oil concentration $C0$, with a uniform volume fraction of the dispersed phase. The radial velocity was assumed to be zero, in consideration of fully developed flow in the inlet section (z=0) of the membrane. The following equation describes the axial velocity:

$$U_z = \frac{Re\mu}{\rho R} \tag{25}$$

$$u = u_0, v = o \; for \; each \; phase \tag{26}$$

$$a_k = a_{k0} \; for \; dispersed \; phase \tag{27}$$

Where y, R, and U_z represent the radial coordinate, the internal radius of the tubular membrane, and the average velocity, respectively. At the feed channel outlet section (Z=L), the pressure was assumed to be equal to atmospheric pressure (1 atm) for both phases.

By neglecting axial diffusion in the membrane and considering symmetry conditions at y=0, the following equations were assumed for the simulation:

$$\frac{\partial v}{\partial y} = 0, \quad \frac{\partial C}{\partial y} = 0, \quad v = 0 \tag{28}$$

$$\frac{\partial u}{\partial x} = 0, \quad \frac{\partial C}{\partial x} = 0 \quad w = 0 \tag{29}$$

For porous membrane:

$$u = 0, \; w = 0, and \;\; v = J_v = \frac{\Delta p}{\mu I R} \tag{30}$$

Figure 1 is the geometry work which was done in COMSOL Multiphysics for an annular membrane which used in this study. In this study, the no-slip boundary condition was considered for all walls and the membrane interface. Feed, as a mixture of water and oil droplet is injected into the tube from the left side of the membrane. Water passes along the tube, and oil permeates through the porous membrane as the product. Simulations are done for a hydrophobic polyvinylidene fluoride (PVDF) membrane with 70% porosity and a PVDF water diffusion coefficient equal to 8.71e^{-11} m^2/s. The oil-in-water emulsion is considered as the injection phase. oil density and viscosity are intended to be 850 kg/m^3 and 0.00332 kg/m.s, respectively. As discussed before, in this study, the feed channel is 30 × 3 × 0.1 cm in height, diameter, and thickness, respectively. The permeate channel has the same shape with a 5 cm inside diameter. The feed is a mixture of water as the continuous phase containing emulsified oil as the dispersed phase in the form of micelles. Figure 2 is a 3D mesh work generated by the use of Comsol Multiphysics for the tubular membrane.

3. Results and discussion

3-1- continuous phase velocity

Figure 2 depicts the velocity magnitude of water as the continuous phase within the feed channel, membrane, and permeate channel of the membrane contactor under conditions of Re=500, TMP=1 bar, and an oil concentration of 500 ppm. The oil-water mixture, characterized by a droplet diameter of 50 µm, enters the feed channel from the left side. The color gradient illustrates the velocity distribution, with higher velocities near the inlet region, decreasing progressively across the membrane's surface. This pattern reflects the flow dynamics under the specified operating conditions, providing insight into the fluid behavior and membrane interaction.

3-2- The Effect of Feed Velocity Injection on Continuous Phase and Dispersed Phase

Figure 3 shows the surface velocity distribution of the continuous phase and the volume fraction distribution of the dispersed phase, under specific operating conditions along the membrane obtained through simulation. These figures illustrate the simulation results under steady-state conditions for different Reynolds numbers ranging from 500 to 2200. Figure 3(a) presents the surface velocity magnitude field of water as the continuous phase, while Figure 3(b) shows the volume fraction of the dispersed phase (oil) inside the membrane. As depicted in both figures, the behavior of the continuous and dispersed phases is significantly influenced by changes in flow velocity within the laminar flow regime. As can be seen in these figures, both the velocity field and the dispersed phase distribution change as the flow velocity increases. These figures also demonstrate that, after a short distance from the membrane module's inlet, a layer of oil begins to form around the membrane. Over time, oil droplets accumulate on the membrane surface, leading to the development of a cake layer. As shown in the figures, this cake layer becomes progressively thicker along the length of the tube. Under steady-state conditions, the thickness of this layer stabilizes and is closely related to the fluid velocity. It is evident from the figures that at lower Reynolds numbers, the oil layer is thicker. However, as the inlet feed velocity increases, this layer becomes thinner. The reason is that higher velocities generate sufficient shear forces to remove the accumulated droplets layers from the membrane surface. Additionally, the outlet velocity increases as the effective flow area decreases due to the growing thickness of the oil cake layer near the exit. Figure 3(b) further reveals that the oil volume fraction decreases along the tube's length, primarily due to the penetration of oil through the membrane.

3-3- Velocity field for continuous phase

Figures 4(a, b) illustrate the changes in the velocity profile of the continuous phase along the annular membrane for four different points inside the tube. These profiles are presented for conditions where Re=3000, TMP=1 bar, the oil concentration is 500 ppm, and the oil droplet diameter is 30 µm.

Figure 4(a) presents the axial velocity magnitude(z-component) of the continuous phase. As expected, the velocity of the continuous phase surface decreases to zero near the pipe wall because the pipe wall is motionless and stationary. Also, in each radius, the velocity magnitude increases by increasing the length from L/4 to L/3 and L/2 and 3L/4. Figure 4(b) shows the time-dependent development of the z-component of the velocity field for the continuous phase at Re=500. The conditions for this simulation include an oil concentration of 500 ppm, Trans Membrane Pressure of 1 bar, and an oil droplet size of 30 µm. As shown in the figure, the velocity profile changes over time until it reaches the developed state. This time-dependent behavior indicates that the velocity field becomes gradually developing with increasing time, reflecting the dynamic nature of the flow as it adjusts to the conditions. The obtained results are consistent with those obtained by other experimental and simulation studies reported by other researchers [44].

3-4 The effect of Reynold Number on Cake Thickness and Permeate concentration:

Figure 5 shows the impact of changing Re number on Cake thickness along the length of the membrane for different Re numbers at 3 bars. A higher Reynolds number indicates a higher flow velocity and a more turbulent flow regime.

Figure 6 presents the effect of Reynolds number (Re) on the permeate concentration profile along the length of the membrane, measured at a transmembrane pressure (TMP) of 3 bar. The figure illustrates how varying the Reynolds number impacts the distribution of permeate concentration across the membrane. At lower Reynolds numbers, the flow velocity of the feed is reduced. This decreased velocity means that the oil droplets and micelles in the feed have a longer residence near the membrane surface, which results in a slower migration from the feed bulk to the membrane channels. It means more time to proceed with their migration from the feed bulk toward the membrane channels.

The longer residence time of the oil droplets and micelles at lower Reynolds numbers leads to a less efficient sweeping effect of the flow. In other words, the flow is less effective at removing these particles from the membrane surface. This inefficiency results in a higher concentration of oil droplets and micelles on membrane surface, leading to a lower peak in the permeate concentration profile.

Conversely, at higher Reynolds numbers, the increased flow velocity enhances the sweeping effect. The higher flow velocity means that the oil droplets and micelles are more effectively transported away from the membrane surface. This results in a lower concentration of these particles on the membrane surface resulting in an increasing the peak in the permeate concentration profile. These results are consistent with both experimental observations and other numerical simulations. [39] which have shown that higher Reynolds numbers lead to higher permeate concentrations due to the increase in the efficiency of removing oil droplets and micelles from the membrane surface. These results are in agreement with previous experimental and numerical studies reported by other researchers [25, 37, 38, 44, 45].

3-5 The effect of oil concentration on the performance of the membrane:

Figure 7 illustrates the effect of oil injection concentration on membrane performance by presenting the variation of cake thickness along the membrane at a constant Reynolds number of 3000 and a TMP of 3 bar. The results clearly show that cake thickness increases with increasing oil concentration in the feed.

These observations align with experimental studies reported in the literature [35], which also found that increasing oil concentration results in higher permeate concentrations and thicker cake layers on the membrane surface.

3-6 The effect of trans membrane pressure (TMP) on the performance of the membrane

Figures 8(a) and 8(b) illustrate the impact of transmembrane pressure (TMP) on membrane performance under different Reynolds numbers and Trans Membrane Pressure with a constant oil concentration of 2000 ppm.

Figure 8(a) shows the relationship between TMP and permeate concentration at different Reynolds numbers (500, 1500, and 3000) with a constant oil concentration of 2000 ppm. Simulation shows that as TMP increases, the permeate concentration also increases. This is because a higher TMP provides stronger filtration, resulting in a greater amount of oil droplets passing through the membrane. The graph indicates that at higher Reynolds numbers, the permeate concentration increases more significantly. This is due to the enhanced flow velocity associated with higher Reynolds numbers, which allows for a higher flux of oil droplets through the membrane. At lower TMPs, the rate at which permeate concentration increases is higher. This suggests that lower TMPs might be more effective in enhancing permeate concentration initially. As TMP continues to increase, the rate of increase in permeate concentration becomes less pronounced, indicating that the relationship between TMP and permeate concentration becomes less sensitive at higher TMPs.

Figure 8(b) shows the Effect of TMP on Cake Thickness along the length of the membrane in a constant Reynolds number (Re = 3000) and oil concentration (C = 2000 ppm). The results demonstrate that increasing TMP leads to a decrease in cake thickness on the membrane surface. This can be attributed to the compressive effects of higher pressure. Higher TMP exerts greater pressure on the membrane, which compresses and compacts the oil droplets and particles in the cake layer. This compression reduces the overall thickness of the oily layer that accumulates on the membrane surface. The compressive force applied by higher TMP reduces the thickness of the cake layer. This occurs because the increased pressure forces the oil droplets closer together, leading to a denser but thinner cake layer.

The observed effects are consistent with experimental findings reported by researchers [39, 45, 47]These studies also showed that higher TMP increases permeate concentration while reducing cake thickness due to the compressive effects on the deposited layer.

3-7 The effect of droplet diameter on the performance of the membrane

Figure 9 shows the relationship between permeation velocity and axial position along the membrane for various oil droplet diameters, at Re= 1500 and TMP=1 bar. These experiments were performed for oil droplets with diameters of 30, 40, and 50 micrometers.

The figure shows that the permeation velocity increases as the oil droplet diameter increases. This indicates that larger oil droplets lead to higher permeation velocities along the membrane. Larger oil droplet size provides a reduction in the specific resistance of polarization layer, which makes it more permeable and results in the increasing in permeate flux. The same results are observed and reported by other researchers, and experimental results [2, 43, 48, 49, 50]. These studies have similarly reported that larger oil droplets reduce the resistance of the polarization layer and thus increase permeate flux.

Larger droplets result in a less dense polarization layer compared to smaller droplets. This reduction in density decreases the resistance to flow through the layer, making it more permeable. With a more permeable polarization layer, the flow of permeate through the membrane is less hindered, resulting in an increased permeation velocity. Smaller oil droplets tend to accumulate and form a thicker, denser polarization layer on the membrane surface. This thicker layer increases the resistance to permeate flow. In contrast, larger droplets are less likely to form such a dense layer, reducing the resistance and allowing for a higher permeation velocity. The reduced resistance at larger droplet sizes leads to improved flow dynamics, which enhances the overall permeation velocity along the membrane.

4. Conclusions

This study demonstrates the effectiveness of COMSOL Multiphysics software as a powerful tool for modeling the performance of a hollow fiber hydrophobic membrane for filtration by using three-dimensional simulations. The simulation employed to model the separation of water, as the continuous phase, from oil as the dispersed phase.

The finite element technique was applied to solve the transport equations of dilute species through the membrane, utilizing Eulerian multi-phase flow theory and Darcy's Law, alongside the porous media model. The results of this investigation provide a comprehensive understanding of how various parameters influence membrane filtration performance.

Additionally, an increase in the injection flow rate significantly raises the concentration of oil in the permeate while simultaneously reducing the thickness of the oil layer. Higher flow rates result in more transport of oil droplets towards the membrane surface, which enhances the overall oil concentration in the permeate and reduces the accumulation of oil on the membrane.

Furthermore, higher oil concentrations in the inlet flow are directly correlated with increased permeate concentration. As the concentration of oil in the feed solution rises, more oil droplets are available to permeate through the membrane, leading to a higher oil concentration in the permeate.

These findings show the importance of key parameters, such as transmembrane pressure, injection flow rate, and oil concentration, on the performance of membrane filtration systems. By adjusting these parameters, it is possible to enhance the efficiency of the filtration process, leading to more effective separation and reduced operational costs. The insights gained from this study are valuable for designing and optimizing membrane filtration systems.

Figures:

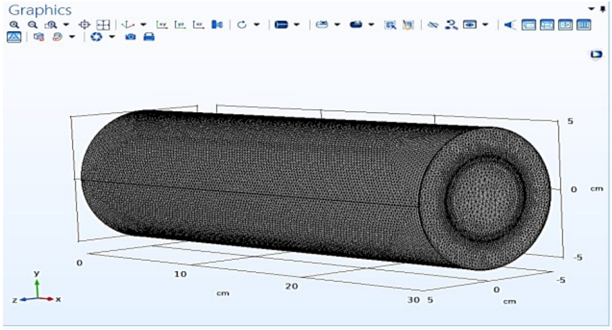

Figure 1. Three-dimensional mesh of the annular membrane.

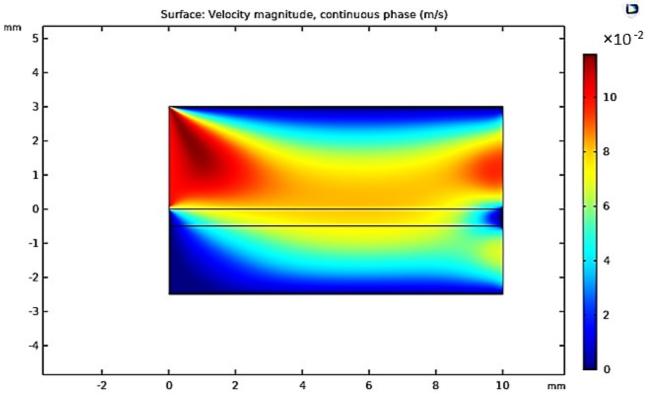

Figure 2. Velocity magnitude field of the continuous phase at a Reynolds number (Re) of 500, an inlet oil concentration of 500 ppm as dispersed phase, and a Trans

Membrane Pressure (TMP) of 1 bar.

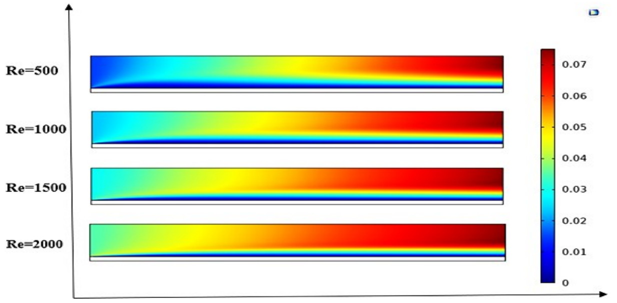

Figure 3(a). Surface velocity magnitude field for the continuous phase under conditions of a Trans Membrane Pressure (TMP) of 1 bar and an inlet oil concentration of 500 ppm and an oil droplet diameter of 30 µm.

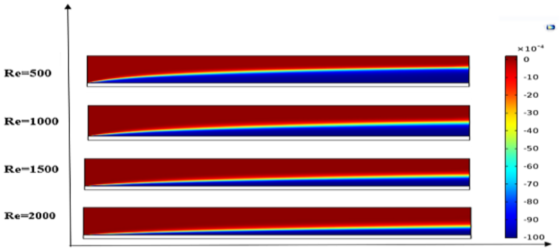

Figure 3(b) Variation of the dispersed phase volume fraction along the membrane under conditions of a Trans Membrane Pressure (TMP) of 1 bar, an inlet oil concentration of 500 ppm, and an oil droplet diameter of 30 µm.

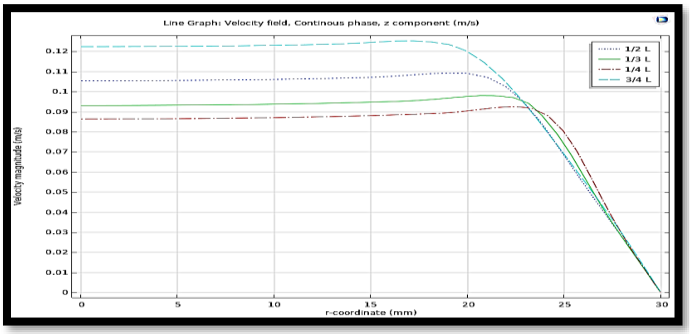

Figure 4(a). Velocity profile for the continuous phase in the z-component as a function of length (L) under the following conditions: Reynolds number (Re) of 3000, concentration of 500 ppm, transmembrane pressure (TMP) of 1 bar, and an oil droplet diameter of 30 µm.

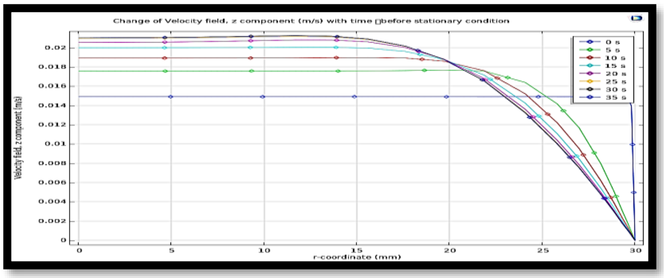

Figure 4(b). Time-dependent velocity field in the z-component under the following conditions: Reynolds number (Re) of 500, concentration of 500 ppm, transmembrane pressure (TMP) of 1 bar, and an oil droplet diameter of 30 µm.

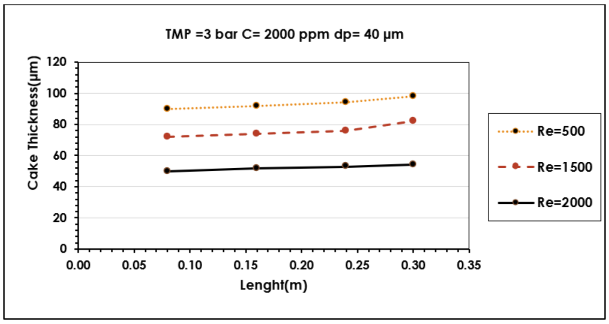

Figure 5. Variation in cake thickness along the length of the membrane for different Reynolds numbers (Re) at a transmembrane pressure (TMP) of 3 bar and oil droplet diameter of 40 µm and inlet concentration of 2000 ppm.

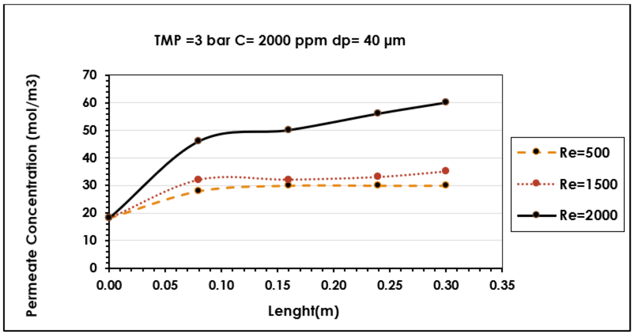

Figure 6. Variation in permeate concentration profile along the length of the membrane for different Reynolds numbers (Re) at a transmembrane pressure (TMP) of 3 bar and oil droplet diameter of 40 µm and inlet concentration of 2000 ppm.

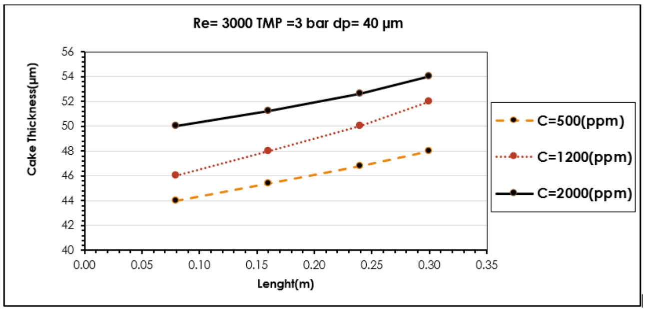

Figure 7. Cake thickness as a function of oil injection concentration along the membrane, for a Reynolds number of 3000 and a transmembrane pressure (TMP) of 3 bar and oil droplet diameter of 40 µm.

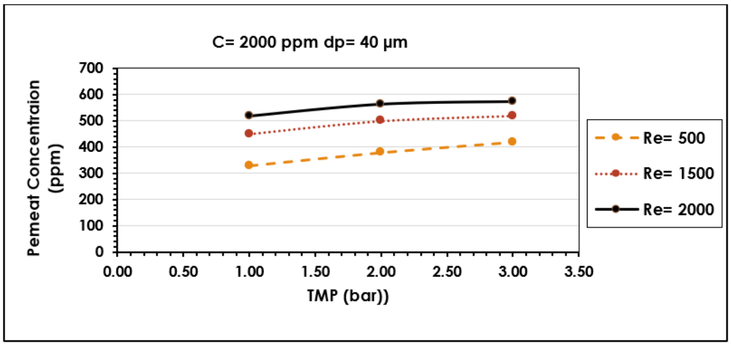

Figure 8(a). Total permeate concentration as a function of transmembrane pressure (TMP) for various Reynolds numbers (Re) at a concentration of 2000 ppm and oil droplet diameter of 40 µm.

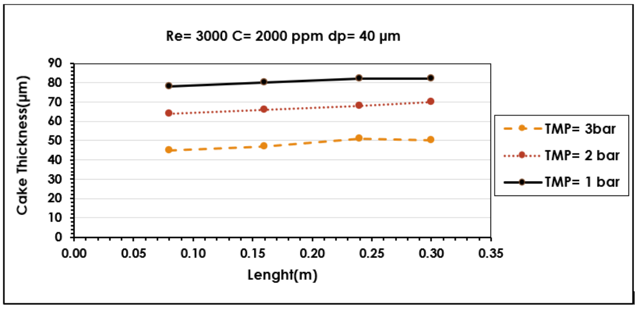

Figure 8(b). Variation of cake thickness as a function of transmembrane pressure (TMP) along the membrane, for a Reynolds number of 3000 and a concentration of 2000 ppm and oil droplet diameter of 40 µm.

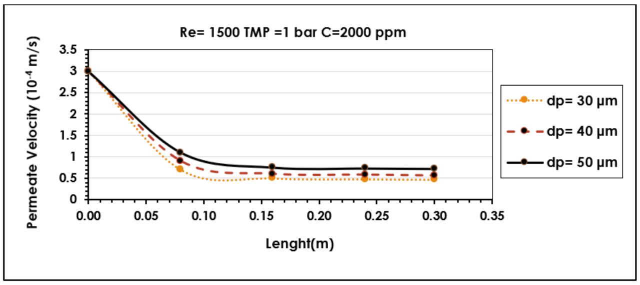

Figure 9. Permeation velocity as a function of axial position along the membrane, presented for varying oil droplet diameters at a Reynolds number (Re) of 1500 and a transmembrane pressure (TMP) of 1 bar. This analysis explores droplet size variations from 30 to 50 micrometers with an inlet concentration of 2000 ppm.

References

[1]. Wang, J.-Y., et al., Enhanced superhydrophobicity and durability of modified cotton cloth for efficient oil-water separation. Separation and Purification Technology, 2025. **354**: p. 128716.

[2]. Sayad, I., et al., Effect of Transducer Position on Droplet Coalescence. Procedia Computer Science, 2023. **224**: p. 349-356.

[3]. Sutar, R.S., et al., Facile approach to fabricate a high-performance superhydrophobic PS/OTS modified SS mesh for oil-water separation. Colloids and Surfaces A: Physicochemical and Engineering Aspects, 2023. **657**: p. 130561.

[4]. Ning, L., et al., Preparation of two kinds of membranes with reverse wettability from waste masks for continuous oil/water separation. Environmental Science: Advances, 2023. **2**(3): p. 473-483.

[5]. de Souza, J.S., et al., Numerical study of oil/water separation by ceramic membranes in the presence of turbulent flow. 2012.

[6]. Sontti, S.G. and A. Atta, Regulation of droplet size and flow regime by geometrical confinement in a microfluidic flow-focusing device. Physics of Fluids, 2023. **35**(1).

[7]. Zare, M., F.Z. Ashtiani, and A. Fouladitajar, CFD modeling and simulation of concentration polarization in microfiltration of oil–water emulsions; Application of an Eulerian multiphase model. Desalination, 2013. **324**: p. 37-47.

[8]. Wang, Z., et al., Bioinspired under-liquid dual superlyophobic surface for on-demand oil/water separation. Langmuir, 2023. **39**(2): p. 870-877.

[9]. Wang, X., et al., Tune wastepaper to hydrophobic membranes through metal-ion-induced lignocellulose nanofibril crosslinking for oil-water separation. Carbohydrate Polymer Technologies and Applications, 2023. **6**: p. 100377.

[10]. Yu, X., et al., Dual-bioinspired fabrication of Janus Micro/nano PDA-PTFE/TiO2 membrane for efficient oil-water separation. Separation and Purification Technology, 2024. **330**: p. 125201.

[11]. Bai, L., et al., Enhanced superhydrophobicity of electrospun carbon nanofiber membranes by hydrothermal growth of ZnO nanorods for oil–water separation. Arabian Journal of Chemistry, 2023. **16**(3): p. 104523.

[12]. Wang, Y., et al., Scalable and switchable CO2-responsive membranes with high wettability for separation of various oil/water systems. Nature Communications, 2023. **14**(1): p. 1108.

[13]. Fernandes Magalhães, H.L., et al., Thermo-Fluid Dynamics Analysis of the Oil-Water Separation Using Ceramic Membrane. Diffusion Foundations, 2019. **24**: p. 37-60.

14. Li, H., et al., Interfacial demulsification and antifouling of oil/water separation membrane by dynamically self-releasing hydroxide ions. Journal of Membrane Science, 2025. **713**: p. 123341.

[15]. Magalhães, H.L.F., et al., Produced water treatment by ceramic membrane: A numerical investigation by computational fluid dynamics. Advances in Mechanical Engineering, 2017. **9**(3): p. 1687814016688642.

[16]. Liang, S., et al., Performance modeling and analysis of a hollow fiber membrane system. Journal of Membrane Science & Technology, 2016: p. 144.

[17]. Cui, Y., et al., A Self-Cleaning TiO2 Bacterial Cellulose Super-Hydrophilic Underwater Super-Oleophobic Composite Membrane for Efficient Oil–Water Separation. Molecules, 2023. **28**(8): p. 3396.

[18]. Mansour, M., et al., Numerical study of the separation of two immiscible liquids in helical and straight pipes. Chemical Engineering and Processing-Process Intensification, 2022. **180**: p. 108654.

[19]. Gong, H., et al., Structural optimization and separation characteristic of a separating device for three phases: Oil, water, and solid. Process Safety and Environmental Protection, 2023. **171**: p. 200-213.

[20]. Chen, W., et al., Framework reinforced orderly-woven superhydrophobic metal–carbon composites for efficient emulsion separation in harsh environments. Separation and Purification Technology, 2024. **330**: p. 125317.

[21]. Rasouli, S., et al., Selective and Continuous Oil Removal from Oil–Water Mixtures Using a Superhydrophobic and Superoleophilic Stainless Steel Mesh Tube. Langmuir, 2023. **39**(11): p. 4100-4112.

[22]. Rana, A., S. Ghosh, and S. Biswas, An eco-friendly approach using a nonfluorous self-cleaning metal–organic framework composite and membrane for oil–water separation. Inorganic Chemistry Frontiers, 2023. **10**(2): p. 612-620.

[23]. Melnik, A., et al., Oil–water separation on hydrophobic and superhydrophobic membranes made of stainless steel meshes with fluoropolymer coatings. Water, 2023. **15**(7): p. 1346.

[24]. Zhang, X., et al., Superhydrophobic and magnetic Fe3O4/RGO/SA composite membranes for oil-water separation. Materials Chemistry and Physics, 2024. **312**: p. 128688.

[25]. Ghadiri, M., A. Marjani, and S. Shirazian, Mathematical modeling and simulation of CO2 stripping from monoethanolamine solution using nano porous membrane contactors. International Journal of Greenhouse Gas Control, 2013. **13**: p. 1-8.

[26]. Shirazian, S., et al., Implementation of the finite element method for simulation of mass transfer in membrane contactors. Chemical engineering & technology, 2012. **35**(6): p. 1077-1084.

[27]. Rezakazemi, M., et al., CFD simulation of natural gas sweetening in a gas–liquid hollow-fiber membrane contactor. Chemical Engineering Journal, 2011. **168**(3): p. 1217-1226.

[28]. Ezazi, M. and M. Quazi, Recent Developments in Two-Dimensional Materials-Based Membranes for Oil–Water Separation. Membranes, 2023. **13**(7): p. 677.

[29]. Akter, F. and U.K. Deb, Computational modeling and dynamics of the oil and water flow using the Galerkin approximation. American Journal of Computational Mathematics, 2017. **7**(01): p. 58-69.

[30]. Heinz, S., J. Heinz, and J.A. Brant, Mass Transport in Membrane Systems: Flow Regime Identification by Fourier Analysis. Fluids, 2022. **7**(12): p. 369.

[31]. Soukane, S., et al., Advanced 3D multiscale modeling of forward osmosis-membrane distillation integrated designs. Desalination, 2024. **571**: p. 117089.

[32]. Razavi, S.M.R., et al., Simulation of CO2 absorption by solution of ammonium ionic liquid in hollow-fiber contactors. Chemical Engineering and Processing: Process Intensification, 2016. **108**: p. 27-34.

[33]. Lin, Q., et al., Self-cleaning photocatalytic MXene composite membrane for synergistically enhanced water treatment: Oil/water separation and dyes removal. Chemical Engineering Journal, 2022. **427**: p. 131668.

[34]. Wang, W., et al., Research on the Performance of a Liquid–Solid Triboelectric Nanogenerator Prototype Based on Multiphase Liquid. Micromachines, 2025. **16**(1): p. 78.

[35]. Yao, M., et al., Enhancing the efficiency of novel PCNF demulsifier for oil-contaminated wastewater treatment through numerical simulation optimization of demulsification mechanism. Journal of Water Process Engineering, 2025. **69**: p. 106626.

[36]. Al-Ammar, Z. and K.E. Amori, Numerical Investigation on Oil/Water Separation by Compact Nozzle-Axial Hydrocyclone. Journal homepage: http://iieta. org/journals/ijht, 2022. **40**(1): p. 71-80.

[37]. Ghasem, N., M. Al-Marsouqi, and N.A. Rahim. Modeling and simulation of membrane contactor employed to strip CO2 from rich solvents via COMSOL Multiphysics®. in Proceedings of the COMSOL Conference. Zurich: COMSL. 2014.

[38]. Shirzadi, M., et al., Prediction of submicron particle dynamics in fibrous filter using deep convolutional neural networks. Physics of Fluids, 2022. **34**(12).

[39]. Keyvan Hosseini, M., Computational Fluid Dynamics (Cfd) Modeling Of A

Pilot-Scale Membrane Filtration Technology To Treat Oily Wastewater. 2022.

[40]. Jalilian, M., et al., An experimental investigation of nanoemulsion enhanced oil recovery: Use of unconsolidated porous systems. Fuel, 2019. **251**: p. 754-762.

[41]. Al-Marzouqi, M.H., et al., Modeling of CO2 absorption in membrane contactors. Separation and Purification Technology, 2008. **59**(3): p. 286-293.

[42]. Patel, M., et al., Membrane-based downhole oil–water separation (DOWS) technology: an alternative to hydrocyclone-based DOWS. Journal of Petroleum Exploration and Production Technology, 2020. **10**: p. 2079-2088.

[43]. Mehmet, O. and S. YAYLA, Effects of Corrugated Plates on Separation Performance. Yüzüncü Yıl Üniversitesi Fen Bilimleri Enstitüsü Dergisi, 2022. **27**(2): p. 286-302.

[44]. Asefi, H., et al., CFD modeling and simulation of concentration polarization reduction by gas sparging cross-flow nanofiltration. Journal of Environmental Chemical Engineering, 2019. **7**(5): p. 103275.

[45]. Li, B., et al., Recent developments in the application of membrane separation technology and its challenges in oil-water separation: A review. Chemosphere, 2023: p. 138528.

[46]. Li, D., et al., Influence of Coalescing Plate Escape Hole Structure on Oil Droplet Escape Performance. Available at SSRN 5087803.

[47]. Liu, H.-S., et al., Wax deposition modeling in oil-water stratified pipe flow. Petroleum Science, 2023. **20**(1): p. 526-539.

[48]. Cheng, X., et al., Biodegradable electrospinning superhydrophilic nanofiber membranes for ultrafast oil-water separation. Science Advances, 2023. **9**(34): p. eadh8195.

[49]. Li, J., et al., Environmental-friendly regenerated lignocellulose functionalized cotton fabric to prepare multi-functional degradable membrane for efficient oil–water separation and solar seawater desalination. Scientific Reports, 2023. **13**(1): p. 5251.

[50]. Ahmadzadeh, S., Torkaman, P., Kalati, S. S., Jafari, A., & Karimzadeh, R. (2023). Environmental effects of enhanced oil recovery methods. Journal of Advanced Environmental Research and Technology, **1**(1), 39–48.